Biosensors and Bioelectronics ■ (■■■■) ■■■–■■■

Contents lists available at ScienceDirect

Biosensors and Bioelectronics

journal homepage: www.elsevier.com/locate/bios

Interlocked graphene–*Prussian blue* hybrid composites enable multifunctional electrochemical applications

Minwei Zhang, Chengyi Hou, Arnab Halder, Jens Ulstrup, Qijin Chi *

Department of Chemistry, Technical University of Denmark, DK-2800 Kongens Lyngby, Denmark

ARTICLE INFO

Article history:
Received 1 December 2015
Received in revised form
13 February 2016
Accepted 16 February 2016

Keywords:
One-pot synthesis
Prussian blue
Graphene
Biosensor
Supercapacitor

ABSTRACT

There has been increasing interest recently in mixed-valence inorganic nanostructure functionalized graphene composites, represented by *Prussian blue*, because they can cost-effectively apply to biosensors and energy devices. In this work, we present a one-pot green method to synthesize interlocked graphene–*Prussian Blue* hybrid composites as high-performance materials for biosensors and supercapacitor electrodes. Given the fact that graphene oxide (GO) can act as an electron acceptor, we used iron(II) and glucose as co-reducing agents to reduce GO under mild reaction conditions without introducing toxic agents. High quality *Prussian blue* nanocubes with no or little coordinated water were generated simultaneously. Reduced graphene oxide (rGO) was thus functionalized by *Prussian blue* nanocubes via chemical bonding to form a kind of interlocked microstructure with high stability and good conductivity. The as-synthesized composites were tested for biosensing of hydrogen peroxide (H_2O_2) and as supercapacitor electrode materials. The specific capacitance of the microcomposite based electrodes can reach 428 F g^{-1}, with good cycling stability. The microcomposite also displays high performance catalysis towards electroreduction of H_2O_2 with a high sensitivity of 1.5 A cm^{-2} M^{-1}.

1. Introduction

Prussian blue (PB), as a non-enzymatic but enzyme mimicking catalyst, has been explored for applications in chemical sensors (Chi and Dong 1995; Liu et al., 2014a, 2014b; Yang et al., 2015a, 2015b; Zhao et al., 2005), biosensors (Arduini et al., 2006; Gao et al., 2014; Sekar et al., 2014; Wang et al., 2014; Zhu et al., 2013), energy devices (Okubo et al., 2010; Pasta et al., 2012) and water quality monitoring (Hao et al., 2015). PB and its analogs are considered as promising energy storage materials, because the theoretical specific capacity of PB can be as high as 170 mA h g^{-1} (Okubo et al., 2010). In addition, the facile synthetic procedure, nontoxicity and low cost of PB based materials make them have potential favoring for large-scale production and multifunctional applications. However, to date these great potentials have been far from exploitation, as the practically achieved specific capacity of PB is much lower than theoretical expectation. PB also suffers from low Coulombic efficiency and poor cycling stability, which has limited its practical utilization as energy materials. This has largely originated in the poor process used in PB crystal growth, in which coordinated water is hardly avoided and occupies most vacancies of the PB crystal. Moreover, the water-occupied vacancies may induce a lattice distortion, which dramatically affects specific capacity and Coulombic efficiency, and deteriorates overall electrochemical performances. In most cases, PB prepared by the direct precipitation reaction of the M^{m+} cations and the $[M(CN)_6]^{n-}$ anions in a neutral aqueous solution always contains a large number of vacancies occupied by coordinated water, because of the fast precipitation process. However, a recent report showed that high-quality PB nanocubes or/and analogs without coordinated water can be synthesized by employing $Na_4Fe(CN)_6$ as a single iron-source precursor, and the resulting material was tested as cathode electrodes for sodium-ion battery with impressive electrochemical performances (Yang et al., 2015a, 2015b; You et al., 2014). This was achieved by a slow process for growth of PB crystals, so that the number of vacancies occupied by coordinated water is dramatically reduced or even completely eliminated in some cases.

Graphene-based materials have captured great attention among physicists, chemists and materials scientists. Graphene is a two-dimensional (2D) sheet of carbon atoms in a hexagonal configuration connected by sp^2 bonds. This unique nanostructure holds considerable promise for its potential applications in many technological fields such as nanoelectronics (Berger et al., 2004; Cernetic et al., 2014), sensors (Dong et al., 2012; Li et al., 2014; Song et al., 2010), functional nanocomposites (Klein et al., 2015; Zhang et al., 2010a, 2010b; Zhu et al., 2013), and energy devices (Liu et al., 2014a, 2014b; Wang et al., 2011; Xiong et al., 2015; Xu

* Corresponding author.
E-mail address: cq@kemi.dtu.dk (Q. Chi).

http://dx.doi.org/10.1016/j.bios.2016.02.044
0956-5663/

et al., 2015; Yang et al., 2011). Graphene has been prepared by a variety of methods, including mechanical exfoliation (Li et al., 2008; Novoselov et al., 2004), modified Hummers' methods (Chen et al., 2009; Compton et al., 2010), and chemical vapor deposition (CVD) (Cernetic et al., 2014; Wu et al., 2011). Among these methods, wet-chemical reduction of exfoliated GO is an efficient approach to large-scale production of graphene nanosheets at low cost. However, the most commonly used methods for reduction of GO are carried out using hydrazine and its derivatives (Domingues et al., 2013; Park et al., 2011) as reducing agents. The use of highly toxic and dangerously unstable hydrazine or dimethylhydrazine to reduce GO is not desirable for many applications. Recently, mild conditions were reported to reduce GO, such as L-ascorbic acid (Zhang et al., 2010a, 2010b), reducing sugars (Zhu et al., 2010) and others. Among many green reducing agents, glucose is of particular interest in reducing GO because of its high ability, relatively low-cost, and enabling environmentally friendly reactions. In this work, we used glucose as a co-reducing agent. Based on the fact that GO is an efficient electron acceptor (Akhavan and Ghaderi, 2012; Salas et al., 2010; Guo et al., 2013), GO can be reduced by electron-rich materials such as metals, metal ions, biomolecules or bacteria. This has been demonstrated by several recent reports (Fan et al., 2011; Guo et al., 2013; Liu et al., 2014a, 2014b; Mei et al., 2012). In general, to obtain rGO based functional hybrid materials two steps including reduction and functionalization are normally involved. For example, PB functionalized graphene materials were prepared by mixed PB nanoparticles (PBNPs) directly with rGO, so that PBNPs were confined by electrostatic attraction in rGO papers (Zhu et al., 2013). Zhang et al. (2012) and Qian et al. (2013) used various reducing agents to reduce GO and Fe^{3+} to prepare rGO-PB hybrid materials. In the present work, we report the preparation of high-quality PB nanocube–rGO hybrids by using $K_4Fe(CN)_6$ as the only iron-source. As schematically illustrated in Fig. 1, simultaneous reduction and functionalization of GO have been achieved by a one-step procedure with the green nature of reactions. The as-synthesized PB nanocubes were wrapped by rGO nanosheets to form an interlocked stable structure. This unique structured microcomposite not only can act as an electron mediator, but also can stabilize PB nanocubes in electrochemical environments, which altogether enables this hybrid materials to hold multifunctional applications.

2. Material and methods

2.1. Materials and reagents

Graphite power (<20 μm, synthetic), H_2O_2 (30%), sulfuric acid (H_2SO_4, 95–97%), hydrochloric acid (HCl, 34.5–36.5%), potassium persulfate ($K_2S_2O_8$, $\geq 99\%$), phosphorus pentoxide (P_2O_5, $\geq 98\%$), potassium permanganate ($KMnO_4$, $\geq 99\%$), hydrochloric acid (HCl, 34.5–36.5%), glucose ($\geq 99\%$) and potassium hexacyanoferrate (II) trihydrate ($K_4[Fe(CN)_6]\cdot 3H_2O$, $\geq 99\%$) were obtained from Sigma-Aldrich. All chemical reagents are of at least analytical grade and were used as received without further purification. Milli-Q water (18.2 Ω cm) was used throughout the experiments.

2.2. Synthesis of G–rGO–PB composite

To synthesize high-quality PB modified rGO (G–rGO–PB), 2 mL GO (1 mg/mL) solution was mixed with 10 mL $K_4Fe(CN)_6$ (10 mM), 2 mL (40 mg/mL) glucose and 1 mL 0.5 M HCl. The mixed solution was stirred for 10 min and then heated at 60 °C in a microwave for 3 h. The raw product was collected and purified by centrifugation and filtration. rGO–PB was prepared in the same procedure but in the absence of glucose and is used as a reference sample.

Other details of experiments, including GO synthesis, optimization of reaction conditions for the composite synthesis, construction of electrochemical electrodes and instrumental methods, are provided in the Supporting Information.

3. Results and discussion

3.1. One-step eco-friendly synthesis of G–PB–rGO composites

High quality and stable GO was prepared by the modified Hummer's method (Zhu et al., 2013). GO was well dispersed in pure water, and its UV–vis spectrum is shown in Fig. 2 (brown curve). We compared the efficiency of glucose and PB precursor for the reduction of GO. In comparison with PB–rGO (Fig. 2), GO was further reduced in the presence of glucose. The glucose–rGO (G–rGO) exhibits an absorption peak at 260 nm, while the PB–rGO retains a shoulder peak at 300 nm due to the n–π* transitions of C=O bonds. This indicates that glucose is a stronger reducing agent for GO reduction. However, PB precursor offers electroactive functionalization of GO, as evidenced by the new absorption peak around 725 nm from the PB component (Zhu et al., 2013). Therefore, we used both PB precursor and glucose as co-reducing agents to simultaneously reduce GO and functionalize rGO in microwave-assisted one-step synthesis to obtain G–PB–rGO composite. To gain more details, Raman spectra were recorded (Fig. S1). The D band of GO, rGO–PB and G–rGO–PB that originated in the defects of graphitic planes is located at 1363, 1363 and 1365 cm^{-1}, respectively; and the G band related to the in-plane vibrations of sp^2 is observed at 1594, 1594 and 1595 cm^{-1}. The I_D/I_G ratio of GO,

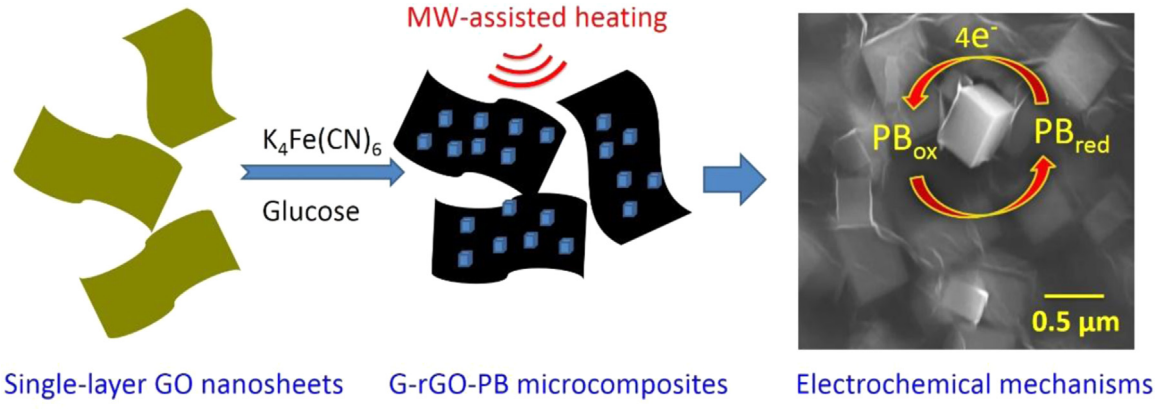

Fig. 1. Schematic representation of the preparation procedure and electrochemical activity of G–rGO–PBs.

Please cite this article as: Zhang, M., et al., Biosensors and Bioelectronics (2016), http://dx.doi.org/10.1016/j.bios.2016.02.044

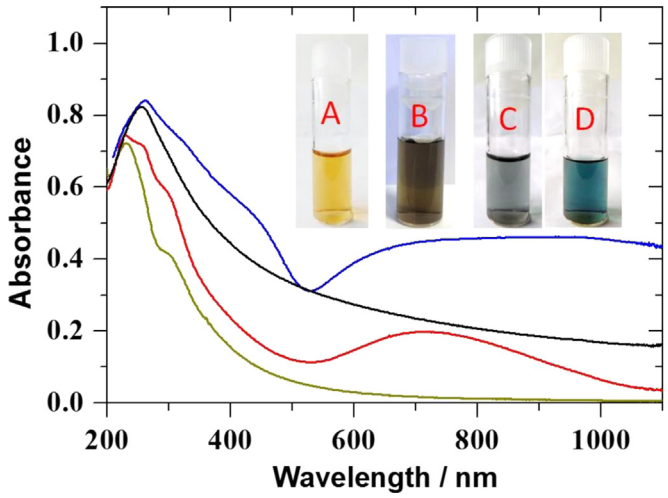

Fig. 2. UV–vis spectra of GO (brown curve), rGO–PB (red curve), glucose reduced graphene oxide (black curve) and G–rGO–PB (blue curve). Insets show digital photographs of GO (A), rGO (B), rGO–PB (C) and G–rGO–PB (D) solutions. (For interpretation of the references to color in this figure legend, the reader is referred to the web version of this article.)

rGO–PB and G–rGO–PB is 1.6, 1.4, and 1.1 respectively, which significantly decreases and indicates that GO was well reduced by the additional presence of glucose to restore the graphitic feature.

The reaction mechanisms are also discussed. Because of its large stability constant ($K_s = 1.0 \times 10^{35}$), $[Fe(CN)_6]^{4-}$ anions are very stable in neutral solutions at room temperature, and almost there is no free Fe^{2+} ions detectable (You et al., 2014). However, Fe^{2+} will get free from $K_4Fe(CN)_6$ crystal in acid media (pH ~ 1.7), and it is then oxidized to Fe^{3+}. The released electrons together with H^+ would react with oxygen-containing groups on GO, leading to the partial reduction of GO to rGO at room temperature. In the meantime, once Fe^{3+} ions were generated, they strongly interacted with carboxyl groups of GO and adsorbed on GO via electrostatic and coordinating interactions (Wang et al., 2012). In other words, this means that Fe^{3+} would be confined (or coordinated) on the surface of GO. Furthermore, the confined Fe^{3+} ions reacted with $[Fe(CN)_6]^{4-}$ to form PB cubes. This enables to form PB nanostructures wrapped with rGO nanosheets. The key reactions could be described by the following chemical equations.

$$GO + K_4Fe(CN)_6 \rightarrow rGO - PB \quad (1)$$

$$GO + nH^+ + ne^- \rightarrow rGO + H_2O \quad (2)$$

$$2Fe^{2+} + 2H^+ \rightarrow 2\,Fe^{3+} + H_2 \quad (3)$$

$$K^+ + Fe^{3+} + [Fe(CN)_6]^{4-} \rightarrow K\{FeFe(CN)_6\} \quad (4)$$

Clearly, this solution-processed procedure allows the formation of PB cubes on GO and GO reduction in one step. The advantages likely include reactions occurred at low temperatures, no toxic reducing agents involved, low cost, and highly conductive composite obtained. To illustrate the $K_4Fe(CN)_6$ role that provides electrons for reduction of GO, different control experiments were designed and performed. Our observations include: (1) GO is not be reduced in the absence of $K_4Fe(CN)_6$ in neutral solutions. (2) The presence of acid is essential for GO reduction by $K_4Fe(CN)_6$. When HCl is at low concentrations or there is no HCl, only very little PB was generated although GO was still partially reduced. This is due to the fact that free Fe^{2+} ions dissociate from $K_4Fe(CN)_6$ only occurs in acidic media. (3) Microwave plays a significant role as well. GO can be reduced by $K_4Fe(CN)_6$ in acid media under room temperature, but it takes much longer (at least 24 h). (4) The introduction of glucose as a co-reducing agent significantly enhanced the conductivity of composites by an improved reduction of GO.

3.2. Structural characterization of G–rGO–PB composites

The as-synthesized composites were examined *first* by powder X-ray diffraction (Fig. S2). In the XRD patterns, the peaks at $2\theta = 17.5°$, 24.8°, 35.3°, 39.6°, and 43.6° correspond to the (2 0 0), (2 2 0), (4 0 0), (4 2 0), and (4 2 2) reflections, respectively. Both rGO–PB and G–rGO–PB patterns exhibit the characteristic diffractions of mixed-valence compound with a face-centered cubic structure (JCPDS card no. 73-0687), which indicates that PB cubes prepared by microwave were highly crystallized. Compared to GO, for rGO–PB samples the peak at $2\theta = 10.5$ almost disappears, which is the evidence that GO was reduced by glucose and Fe^{2+}. To further investigate the interaction between PB and rGO, PB was prepared by directly mixed $FeCl_3$ with $K_4[Fe(CN)_6]$, as shown in Fig. S2, the diffraction peaks for such samples are broadening with lower intensity due to the smaller size of powder particles and poor crystallinity. The diffraction peaks of all rGO–PB samples are found to have a slight shift, which may be due to the distortion of PB lattices arising from the vacancies occupied by coordinated water in PB. It shows that high-quality PB nanocubes with a small number of vacancies and low interstitial water content were prepared by using $K_4Fe(CN)_6$ as the only iron-source. The samples were *further* analyzed by X-ray photoelectron spectroscopy (XPS). The results are offered in the Supporitng Information (Figs. S3, S4 and S5). The XPS spectrum of GO shows intensive O 1s but relatively weak C 1s peaks, and the C 1s XPS spectrum of GO confirms various oxygen-containing groups (OCGs) such as C=O and C–O existing on GO, which indicates that GO has abundant OCGs on the surface of GO sheet. The ratio of C/O was determined as about 3:2. The XPS survey spectra of G–rGO–PB show that, not only O 1s peak significantly decreases and C 1s peak obviously increases, but also the peaks at 398.3 eV corresponding to N 1s and peaks at 708.2 eV corresponding to Fe 2p are observed, which suggests the introduction of PB nanocubes into rGO planes. The C 1 s XPS spectrum of G–rGO–PB shows different carbon atoms in different functional groups: the non-oxygenated ring C/(C–C) (284.7 eV), the C in C–O bonds (286.8 eV), and the carboxylate carbon (C=O) (287.6 eV). The main peak at 284.8 eV was clearly seen, an indicative of only partial reduction of GO. Compared to GO, the signal of C–O in the C 1 s spectrum of G–rGO–PB becomes much weaker, and the calculated ratio of C/O changed to about 2:1. These results conclude that considerable deoxygenation occurred by glucose and Fe^{2+} reduction, resulting in the recovery of graphitic planes on rGO, where a number of OCGs remain on the graphene plane that can serve as the anchoring sites for the growth of PB nanocubes. The high-resolution Fe 2p spin–orbit doublet spectra of PB/rGO composites were recorded. The binding energies of Fe p3/2 and Fe 2p1/2 were observed at 712.3 and 721.2 eV, respectively, which correspond to the Fe^{3+} ions. The peak at 708.4 eV is due to Fe^{2+} 2p3/2 in PB cubes. The ratio of Fe^{3+}/Fe^{2+} was determined as approximately 1.6–0.9, which is largely expected for PB materials. These results confirm the formation of PB that has well-defined crystalline structure. The high-resolution N 1s spectra of G–rGO–PB are deconvoluted into three peaks with the binding energy of 397.5, 399.5, and 403.1 eV, respectively. The peak at 397.5 eV can be attributed to Fe–C≡N bonds of PB cubes, and other peaks (including pyrrolic N2 and pyridine N-oxide N3) reflect the diverse forms of nitrogen functional groups. The peak for Fe–C≡N is predominant in intensity, suggesting that nitrogen atoms detected are mainly from PB.

Microscopy techniques were also used to characterize the

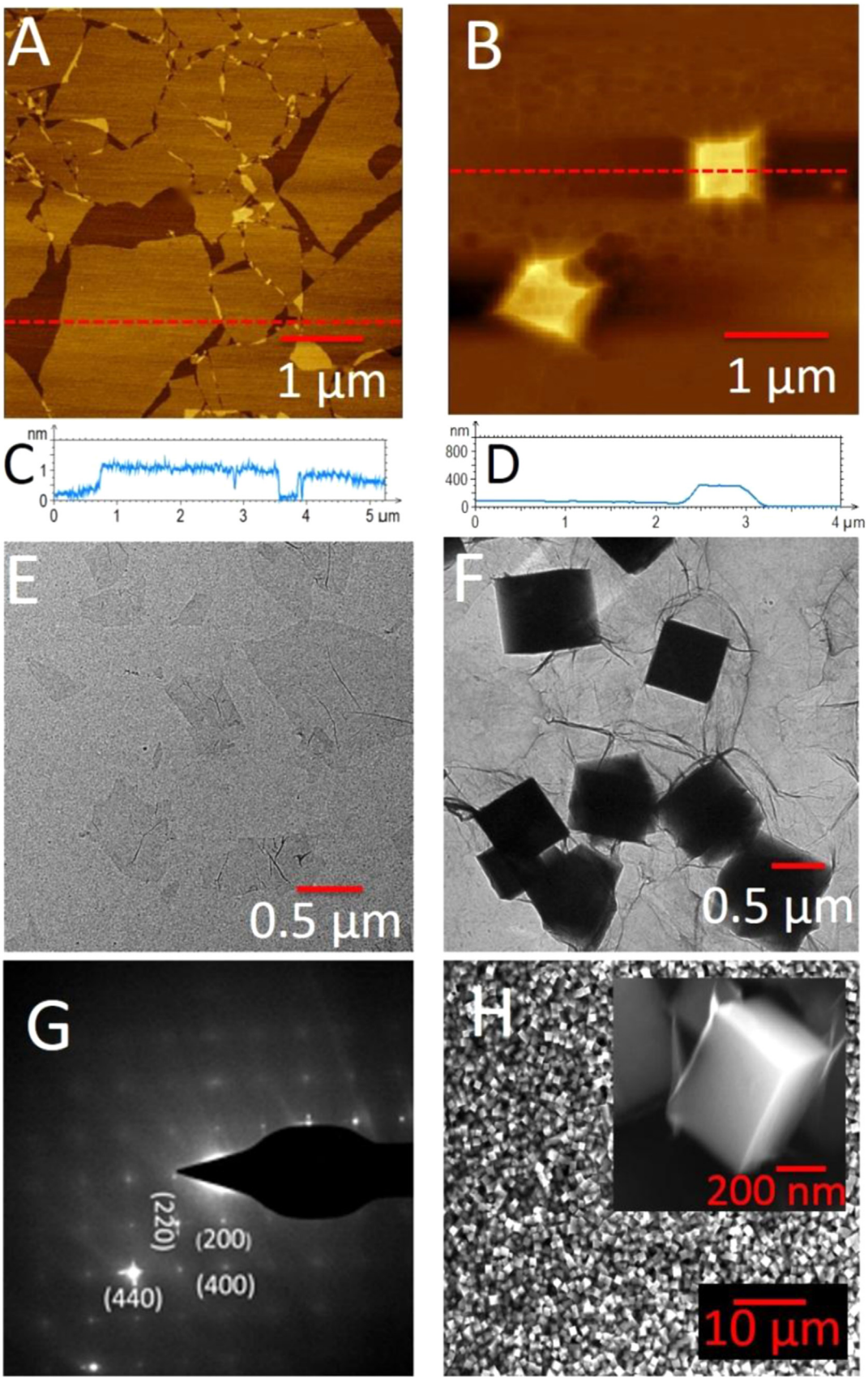

Fig. 3. AFM (A) and TEM (E) images of single layer GO; (C) and (D) cross-sectional profiles of GO and G–rGO–PB; AFM (B) and TEM (F) images of G–rGO–PB. (G) Corresponding SAED pattern of G–rGO–PB. (H) SEM images of G–rGO–PB.

Please cite this article as: Zhang, M., et al., Biosensors and Bioelectronics (2016), http://dx.doi.org/10.1016/j.bios.2016.02.044

structures of samples. As we expected, single layer GO sheets with the lateral dimension in the range of 0.5–5 μm were firstly obtained, as indicated by AFM (Fig. 3A) and TEM images (Fig. 3E). In comparison, as can be seen in FE-SEM images of the final product, G–rGO–PB (Fig. 3), high quality cubic PB nanocrystals with regular cubic shape and the size about 500 nm was wrapped by rGO nanosheets. Comparing SEM images of PB (Fig. S7) with those for rGO–PB (Fig. S6) and G–rGO–PB (Fig. 3), it is found that the size distribution of PB nanocubes wrapped by rGO is more uniform than naked PB cubes. The most likely reason is that Fe^{3+} was locked by –OOH groups and GO induced the directed growth of PB crystals on its surface. In contrast, the growth of PB crystals in the absence of GO nanosheets took place randomly. AFM and TEM images thus confirm the presence of distributed PB nanocubes in graphene matrix (Fig. 2). A TEM image of nanocubes with regular cubic shape is shown in Fig. 3F. The selected area electron diffraction (SAED) pattern (Fig. 3G) taken from an individual nanocube can be indexed to the (2 0 0), (2 2 0), (4 0 0) and (4 4 0) lattice planes of PB, which confirms that the PB nanocubes in the rGO–PB composite are single-crystalline. This result is clearly consistent with XRD analysis (Fig. S2).

Moreover, there were no isolated PB nanocubes observed, but all PB nanocubes were interlocked by the rGO sheets—that can be found in all samples, indicating the formation of rGO–PB composites (Figs. 3 and S6). The results demonstrate that the PB nanocubes can be embedded into a graphene matrix consisting of individual rGO nanosheets, leading to a highly stable interlocked composite structure.

In order to investigate the elemental distribution in G–rGO–PB composites, scanning electron microscopy (SEM) and mapping analysis were performed. SEM mapping images of C, O, and Fe elements are provided in the Supporting Information (Fig. S8). All atoms were distributed uniformly in the composite, and it is also suggested that PB nanocubes have a high distributed coverage on rGO sheets.

3.3. Electroactivity of G–rGO–PB composites

To study the electrochemical behavior of G–rGO–PB hybrid nanomaterials, the as-prepared PB, rGO–PB, and G–rGO–PB electrodes were evaluated by a three-electrode configuration in 0.1 M KCl aqueous electrolyte with the potential window of −0.4 to 0.8 V and the scan rate of 50 mV s^{-1}. Representative cyclic voltammograms (CVs) were compared in Fig. 4. The CV of pure rGO electrodes shows nearly rectangular shape, suggesting ideal electrical double-layer capacitive (EDLC) behavior. The PB, rGO–PB and G–rGO–PB electrodes display evident redox couples with reversible redox peak profiles. The pair of redox peaks are observed at the formal potential of around 0.21 V (vs SCE), as expected for PB materials. In addition to the redox peaks from the PB, the CVs of rGO–PB and G–rGO–PB electrodes also show the significant expansion rectangular capacitive responses with much boosted current, revealing the effective combination of the electroactive component (PB) and capacitive rGO component. Although PB, rGO–PB and G–rGO–PB electrodes show comparably high electrochemical activity, their electron transfer kinetics are notably different. The peak separation (ΔE_P) of PB, rGO–PB and G–rGO–PB was found to be 0.49, 0.11 and 0.10 V at a scan rate of 50 mV/s, respectively. And the rate constant (k_s) was calculated by the Laviron method as 0.04 s^{-1}, 3.8 s^{-1}, and 65 s^{-1} corresponding to PB,

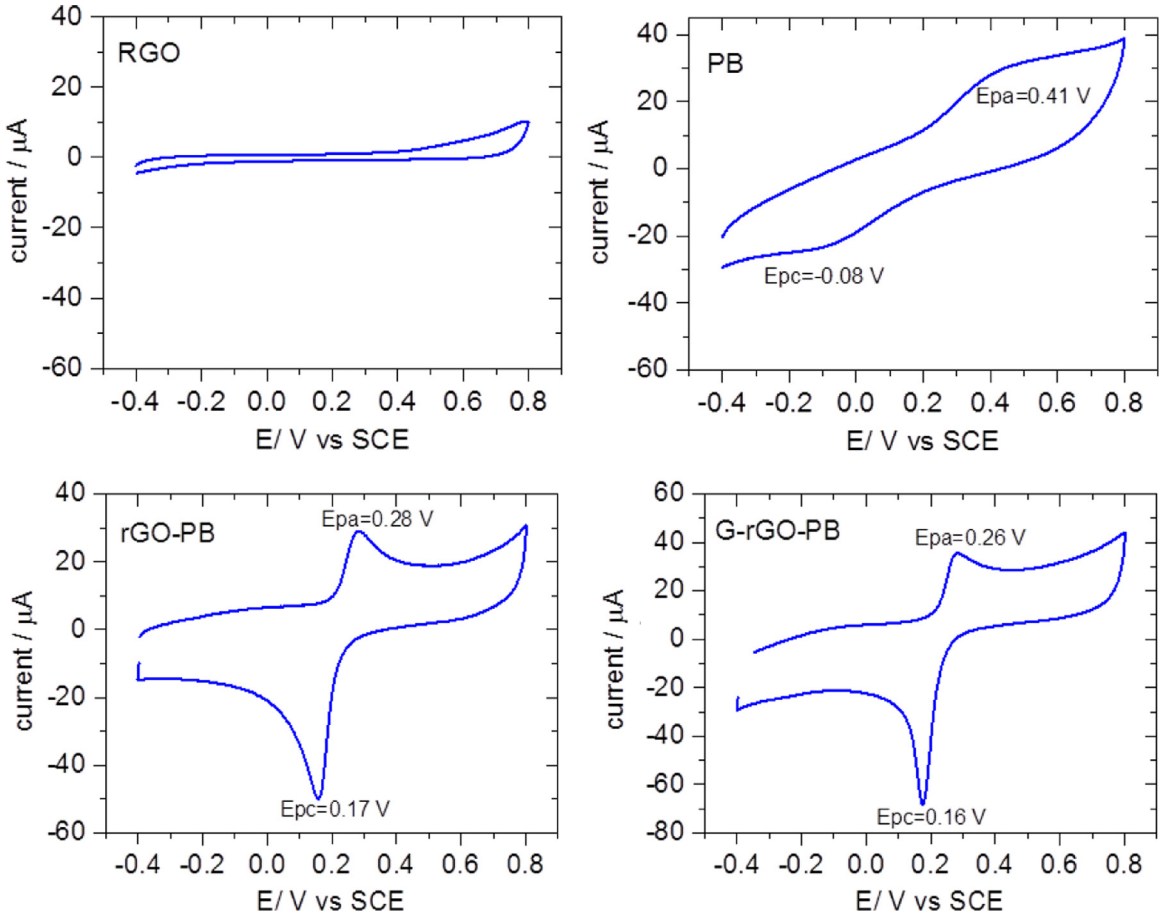

Fig. 4. Cyclic voltammograms of different materials based electrodes in Ar-saturated 0.1 M KCl, obtained with a scan rate of 50 mV/s.

rGO–PB and G–rGO–PB, respectively (Jensen et al., 2009). These results demonstrate that the overpotential of redox process of the Fe(II/III) at G–rGO–PB electrode is notably lowered and the electron transfer rate is significantly enhanced, because GO was highly reduced in the presence of glucose to improve electrical conductivity, and further PB nanocubes were attached to rGO to a synergistic hybrid network favouring electronic coupling for interfacial electron transfer. In order to further investigate the electrochemical behavior of G–rGO–PB hybrid composites, PB and G–rGO–PB electrodes were tested further by electrochemical impedance spectroscopy (EIS) with the results compared in Fig. S10. The EIS spectra were fitted with the appropriate equivalent circuits. Due to all PB cubes were networked by rGO sheets, the charge transfer resistance (Rct) of G–rGO–PB (~0.09 kΩ) is at least a 60-fold lower than that for pure PB cubes (~6.7 kΩ). This observation is consistent with the results obtained from CVs (Fig. 4) and also suggests that G–rGO–PB is a promising material for supercapacitor electrodes or as building blocks for electrochemical sensors, both of which have been tested.

3.4. Application of hybrid composites

3.4.1. Supercapacitor electrodes

The CVs of as-prepared PB, rGO–PB and G–rGO–PB in 1 M KCl electrolyte with the potential window from −0.4 to 0.8 V (versus SCE) were recorded (Supporting Information Fig. S9). The capacitive performance of G–rGO–PB electrodes was further investigated with galvanostatic charge–discharge cycles. Figs. 5A and S11 compare charge–discharge curves of pure PB, rGO–PB and G–rGO–PB electrodes at different applied current densities. The specific capacitance (C_{sp}) of respective materials was calculated from the discharge curves (with the details described in Supporting Information) under different experimental conditions, and the results are compared in Tables 1 and S1. PB and its analogs are considered as promising energy storage materials, because of their high theoretical capacity. In our tests, however, the C_{sp} of pure PB materials is very low, only 4.42 F g^{-1} even at a low current density of 0.25 A g^{-1} (Tables 1 and S1) as well as poor cycling stability was observed (Fig. 5B). This is mainly due to its poor conductivity and limited stability in neutral solutions. In contrast, the C_{sp} of G–rGO–PB electrodes at 0.25 A g^{-1} can reach 428.83 ± 5 F g^{-1}, which is significantly higher if compared to pure rGO (14.7 F g^{-1}) and rGO–PB (165.83 ± 2 F g^{-1}) under the present testing conditions. This is because rGO nanosheets not only can interlock PB cubes but also can enhance the overall conductivity. In addition, G–rGO–PB electrodes show good cycling performance. For example, after 1000 continuous charge–discharge cycles at 2 A/g, C_{sp} was maintained at about 94% (238.13 F g^{-1}) of the initial capacitance. In the same condition, pure PB only retained approximately 50% of its specific capacitance. The results suggest that rGO not only served as electrically conductive support but also protected PB and improved PB stability in electrochemical environments. In addition, the C_{sp} of G–rGO–PB is higher than the theoretical capacity of pure PB. The significant enhancement in electrochemical performance by G–rGO–PB composite is attributed to positive synergetic interactions between the two components, in which the PB nanocubes contribute large pseudo-capacitance and rGO offers high electric double-layer capacitance and conductance.

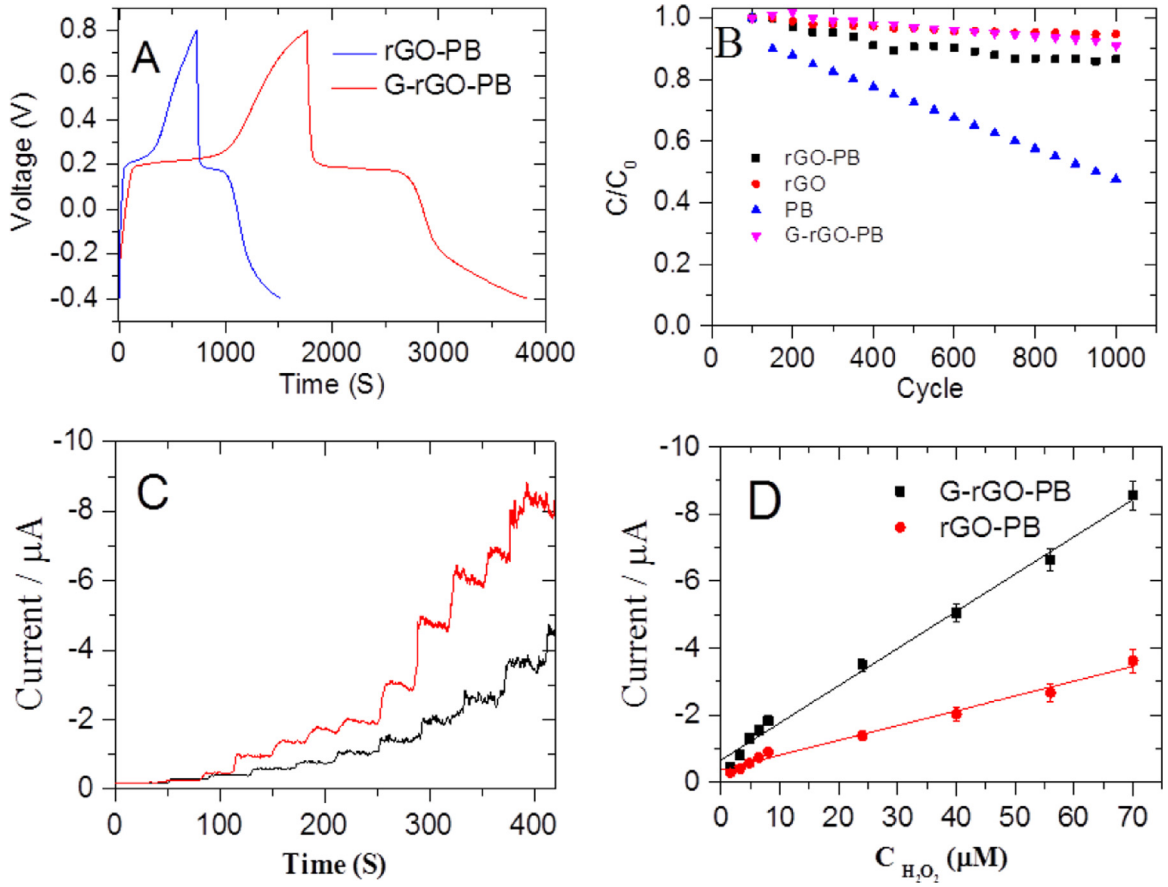

Fig. 5. Electrochemical performances of hybrid composites: (A) charge–discharge curves of rGO–PB (blue curve) and G–rGO–PB (red curve) in Ar-staturated 1 M KCl solution at 0.25 A g^{-1}. (B) Cycling stability of supercapacitor electrodes (C_{sp} vs the number of cycles). (C) Amperometric responses of the rGO–PB (black curve) and G–rGO–PB (red curve) electrodes to successive additions of H_2O_2 at −0.10 V into the stirred Ar-saturated 0.1 M KCl solution. (C) The calibration curves of the current response to different concentrations of H_2O_2. (For interpretation of the references to color in this figure legend, the reader is referred to the web version of this article.)

Please cite this article as: Zhang, M., et al., Biosensors and Bioelectronics (2016), http://dx.doi.org/10.1016/j.bios.2016.02.044

Table 1
Comparison of specific capacitance and energy density obtained with various materials and current densities applied.

Materials	Current density applied ($A\,g^{-1}$)	Specific capacitance ($F\,g^{-1}$)	Energy density ($W\,h\,kg^{-1}$)
PB	1.00	1.17	0.42
	0.25	4.48	1.60
rGO	1.00	1.47	0.53
	0.25	11.04	3.98
rGO–PB	1.00	40	14.40
	0.25	165.83	59.7
G–rGO–PB	1.00	385	138.60
	0.25	428.83	154.38

3.4.2. Biosensing electrocatalysis

To qualitatively evaluate the electroactalysis activity, CVs of the rGO–PB and G–rGO–PB sensors in 0.1 M KCl solutions containing 500 μM H_2O_2 were *first* recorded. Representative CVs are compared in Fig. S12. While electrocatalytic reduction of H_2O_2 by rGO–PB started at 0.2 V (vs SCE) and tended to reach a maximum current at potentials more negative than −0.1 V, G–rGO–PB invoked electrocatalytic reduction of H_2O_2 started at 0.3 V (vs SCE) with a maximum response at potentials more negative than −0.1 V. In order to quantitatively evaluate the performance of electrocatalytic sensing to H_2O_2, both chronoamperometry and differential pulse voltammetry (DPV) were used in measurements. Chronoamperometric responses were recorded at −0.1 V with successive additions of H_2O_2. Typical current–time curves are shown in Fig. 5C. Both rGO–PB and G–rGO–PB electrodes displayed steady-state responses upon successive addition of H_2O_2. A subsequent addition of H_2O_2 to a stirring 0.1 M KCl solution resulted in a remarkable increase in the reduction current, which shows the electrocatalytic activity of the modified electrodes towards the reduction of H_2O_2. The linear relationship between the H_2O_2 concentration and catalytic current is found in the range of 1.6–70 μM at G–rGO–PB electrodes (Fig. 5D), with a detect limit of 0.5 μM. The linear regression equation with a high correlation coefficient (R) of 0.998 is obtained, and the sensitivity is estimated as 1.5 $A\,cm^{-2}\,M^{-1}$, over 3 fold higher than that for rGO–PB ($\approx 0.5\,A\,cm^{-2}\,M^{-1}$). The DPV results are provided in the Supporting Information (Fig. S13). The linear relationship between the H_2O_2 concentration and catalytic current (−0.3 V vs SCE) is found in the range of 2.5–475 μM at G–rGO–PB electrodes (Fig. S13B), with a detect limit (LOD) of 1 μM. The linear regression fit with a high correlation coefficient (R) of 0.991 is obtained, and the sensitivity is estimated as 0.25 $A\,cm^{-2}\,M^{-1}$. Compared the results obtained with chronoamperometric detections, DPV can expand of the linear dynamic range, but the sensitivity is reduced at least by 6 folds. This suggests that chronoamperometric technique is a more effective approach for detection of H_2O_2 using G–rGO–PB as electrocatalyst.

To further verify the performance, some characteristic tests of G–rGO–PB composites were performed. The relative standard deviation for 3 repeated measurements of 50 μM H_2O_2 was 3.4%, which illustrated that the electrochemistry response of G–rGO–PB toward the reduction of H_2O_2 was highly reproducible. In order to explore the specific detection of H_2O_2 using the present materials, the interferences of common ions (1 mM Na^+, Mg^{2+}, and Ca^{2+}) and small molecules (e.g. dopamine, urea acid and ascorbic acid) were investigated. The non-enzymatic chronoamperometric detections of 10 μM H_2O_2 were performed at −0.1 V with successive additions of H_2O_2 and possible interference species. The typical current–time curve shown in Fig. S14 suggests that no significant interference for determination of H_2O_2 was detected upon the presence of these selected ions and compounds. Thus, the composite holds potential for use of detections of H_2O_2 in practical mixture samples. Moreover, for most PB based electrochemical electrochemical sensors Nafion is often used to protect the material and to eliminate redox interferences. However, the Nafion film could slow down interfacial electron transfer between PB and support electrode as well as affect mass transportation of analytes. In the present case, the composite is prepared in the form of interlocked structures. Such structural configuration not only can stabilize PB cubes but also appears to improve the selectivity of H_2O_2 detection. The key performances of G–rGO–PB composites for non-enzymatic detection of H_2O_2 are further compared to those related materials previously reported (Table S2).

4. Conclusions

A novel, green and low-cost method has been explored in this work to prepare high quality *Prussian blue* nanostructure decorated graphene hybrid materials. Graphene oxide is able to be reduced without use of any toxic reagents under mild conditions (low temperature, green reducing agent), accompanied by the formation of PB nanocubes in the one-step procedure. High quality *Prussian blue* nanocubes with a regular cubic shape and approximately 500 nm are wrapped by rGO nanosheets to form interlocked stable composite. The possible reaction mechanisms are discussed in detail. Interlocked graphene–*Prussian Blue* nanocomposites display high performances, when they are tested in biosensing elecrocatalysis and as supercapacitor electrode material. Such structural configuration is intriguing. It can not only stabilize PB cubes but also offer the high selectivity of H_2O_2 detection and high specific capacitance and charge–discharge cycling stability. Therefore, such hybrid composites could be a promising candidate for multiple electrochemical applications, particularly in building Nafion-free electrochemical sensors and high-performance supercapacitor electrodes.

Acknowledgments

This work was supported by the Danish Research Council for Technology and Product Science (Project no. 12-127447). M.Z. acknowledges the CSC Ph.D. scholarship (201306170047). C.H. is grateful to the Ørsted-Marie-Curie cofunded postdoc fellowship.

Appendix A. Supplementary material

Supplementary data associated with this article can be found in the online version at http://dx.doi.org/10.1016/j.bios.2016.02.044

References

Akhavan, O., Ghaderi, E., 2012. Carbon 50, 1853–1860.
Arduini, F., Ricci, F., Tuta, C.S., Moscone, D., Amine, A., Palleschi, G., 2006. Anal. Chim. Acta 580, 155–162.
Berger, C., Song, Z.M., Li, T.B., Li, X.B., Ogbazghi, A.Y., Feng, R., Dai, Z.T., Marchenkov, A.N., Conrad, E.H., First, P.N., de Heer, W.A., 2004. J. Phys. Chem. B 108, 19912–19916.
Cernetic, N., Wu, S.F., Davies, J.A., Krueger, B.W., Hutchins, D.O., Xu, X.D., Ma, H., Jen, A.K.Y., 2014. Adv. Funct. Mater. 24, 3464–3470.
Chen, C., Yang, Q.H., Yang, Y., Lv, W., Wen, Y., Hou, P.X., Wang, M., Cheng, H.M., 2009. Adv. Mater. 21, 3007–3011.
Chi, Q., Dong, S.J., 1995. Anal. Chim. Acta 310, 429–436.
Compton, O.C., Dikin, D.A., Putz, K.W., Brinson, L.C., Nguyen, S.T., 2010. Adv. Mater. 22, 892–896.
Domingues, S.H., Kholmanov, I.N., Kim, T., Kim, J., Tan, C., Chou, H., Alieva, Z.A., Piner, R., Zarbin, A.J.G., Ruoff, R.S., 2013. Carbon 63, 454–459.
Dong, X.C., Xu, H., Wang, X.W., Huang, Y.X., Chan-Park, M.B., Zhang, H., Wang, L.H.,

Huang, N., Chen, P., 2012. ACS Nano 6, 3206–3213.
Fan, Z.J., Kai, W., Yan, J., Wei, T., Zhi, L.J., Feng, J., Ren, Y.M., Song, L.P., Wei, F., 2011. ACS Nano 5, 191–198.
Gao, Z.D., Qu, Y., Li, T., Shrestha, N.K., Song, Y.Y., 2014. Sci. Rep. -UK 4, 6891.
Guo, P., Xiao, F., Liu, Q., Liu, H., Guo, Y., Gong, J.R., Wang, S., Liu, Y., 2013. Sci. Rep. -UK 3, 3499.
Hao, J., Yang, W., Zhang, Z., Tang, J., 2015. Nanoscale 7, 10498–10503.
Jensen, P.S., Chi., Q., Zhang, J., Ulstrup, J., 2007. J. Phys. Chem. C. 113, 13993–14000.
Klein, M., Varvak, A., Segal, E., Markovsky, B., Pulidindi, I.N., Perkas, N., Gedanken, A., 2015. Green Chem. 17, 2418–2425.
Li, S.J., Xia, N., Lv, X.L., Zhao, M.M., Yuan, B.Q., Pang, H., 2014. Sens. Actuat. B – Chem. 190, 809–817.
Li, X., Zhang, G., Bai, X., Sun, X., Wang, X., Wang, E., Dai, H., 2008. Nat. Nanotechnol. 3, 538–542.
Liu, C.Y., Hao, F., Zhao, X.C., Zhao, Q.C., Luo, S.P., Lin, H., 2014a. Sci. Rep. -UK 4, 6898.
Liu, L., Shi, L., Chu, Z., Peng, J., Jin, W., 2014b. Sens. Actuat. B: Chem. 202, 820–826.
Mei, X.G., Zheng, H.Q., Ouyang, J.Y., 2012. J. Mater. Chem. 22, 9109–9116.
Novoselov, K.S., Geim, A.K., Morozov, S.V., Jiang, D., Zhang, Y., Dubonos, S.V., Grigorieva, I.V., Firsov, A.A., 2004. Science 306, 666–669.
Okubo, M., Asakura, D., Mizuno, Y., Kim, J.D., Mizokawa, T., Kudo, T., Honma, I., 2010. J. Phys. Chem. Lett. 1, 2063–2071.
Park, S., An, J., Potts, J.R., Velamakanni, A., Murali, S., Ruoff, R.S., 2011. Carbon 49, 3019–3023.
Pasta, M., Wessells, C.D., Huggins, R.A., Cui, Y., 2012. Nat. Commun. 3, 1149.
Qian, L., Zheng, R., Zheng, L., 2013. J. Nanopart. Res. 15, 1806–1814.
Salas, E.C., Sun, Z., Luttge, A., Tour, J.M., 2010. ACS Nano 4, 4852–4856.
Sekar, N.C., Shaegh, S.A.M., Ng, S.H., Ge, L., Tan, S.N., 2014. Sens. Actuat. B: Chem. 204, 414–420.
Song, Y., Qu, K., Zhao, C., Ren, J., Qu, X., 2010. Adv. Mater. 22, 2206–2210.
Wang, G., Chen, L., Zhu, Y., He, X., Xu, G., Zhang, X., 2014. Analyst 139, 5297–5303.
Wang, L., Ye, Y.J., Zhu, H.Z., Song, Y.H., He, S.J., Xu, F.G., Hou, H.Q., 2012. Nanotechnology 23, 539–545.
Wang, Y., Tong, S.W., Xu, X.F., Ozyilmaz, B., Loh, K.P., 2011. Adv. Mater. 23, 1514–1518.
Wu, Y.Q., Lin, Y.M., Bol, A.A., Jenkins, K.A., Xia, F.N., Farmer, D.B., Zhu, Y., Avouris, P., 2011. Nature 472, 74–78.
Xiong, J., Zhu, W.S., Li, H.P., Ding, W.J., Chao, Y.H., Wu, P.W., Xun, S.H., Zhang, M., Li, H.M., 2015. Green Chem. 17, 1647–1656.
Xu, G.Y., Han, J.P., Ding, B., Nie, P., Pan, J., Dou, H., Li, H.S., Zhang, X.G., 2015. Green Chem. 17, 1668–1674.
Yang, D.Z., Xu, J., Liao, X.Z., Wang, H., He, Y.S., Ma, Z.F., 2015a. Chem. Commun. 51, 8181–8184.
Yang, X.W., Zhu, J.W., Qiu, L., Li, D., 2011. Adv. Mater. 23, 1514–1518.
Yang, Y., Cao, Y., Wang, X., Fang, G., Wang, S., 2015b. Biosens. Bioelectron. 64, 247–254.
You, Y., Wu, X.L., Yin, Y.X., Guo, Y.G., 2014. Energy Environ. Sci. 7, 1643–1647.
Zhang, J.L., Yang, H.J., Shen, G.X., Cheng, P., Zhang, J.Y., Guo, S.W., 2010a. Chem. Commun. 46, 1112–1114.
Zhang, L., Zhang, A., Du, D., Lin, Y., 2012. Nanoscale 4, 4674–4679.
Zhang, Y., Tang, Z.R., Fu, X., Xu, Y.J., 2010b. ACS Nano 4, 7303–7314.
Zhao, G., Feng, J.J., Zhang, Q.L., Li, S.P., Chen, H.Y., 2005. Chem. Mater. 17, 3154–3159.
Zhu, C., Guo, S., Fang, Y., Dong, S., 2010. ACS Nano 4, 2429–2437.
Zhu, N., Han, S., Gan, S.Y., Ulstrup, J., Chi, Q., 2013. Adv. Funct. Mater. 23, 5297–5306.

Please cite this article as: Zhang, M., et al., Biosensors and Bioelectronics (2016), http://dx.doi.org/10.1016/j.bios.2016.02.044